

## Supramolecular Assembly of Halide Perovskite Building Blocks

Cheng Zhu,<sup>#</sup> Jianbo Jin,<sup>#</sup> Mengyu Gao,<sup>#</sup> Alexander M. Oddo, Maria C. Folgueras, Ye Zhang, Chung-Kuan Lin, and Peidong Yang\*Cite This: <https://doi.org/10.1021/jacs.2c04357>

Read Online

ACCESS |



Metrics &amp; More

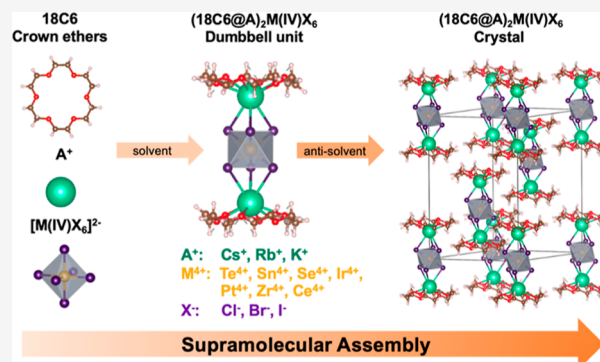


Article Recommendations



Supporting Information

**ABSTRACT:** The structural diversity and tunable optoelectronic properties of halide perovskites originate from the rich chemistry of the metal halide ionic octahedron  $[MX_6]^{n-}$  ( $M = Pb^{2+}$ ,  $Sb^{3+}$ ,  $Te^{4+}$ ,  $Sn^{4+}$ ,  $Pt^{4+}$ , etc.;  $X = Cl^-$ ,  $Br^-$ , and  $I^-$ ). The properties of the extended perovskite solids are dictated by the assembly, connectivity, and interaction of these octahedra within the lattice environment. Hence, the ability to manipulate and control the assembly of the octahedral building blocks is paramount for constructing new perovskite materials. Here, we propose a systematic supramolecular strategy for the assembly of  $[MX_6]^{n-}$  octahedra into a solid extended network. Interaction of alkali metal-bound crown ethers with the  $[M(IV)X_6]^{2-}$  octahedron resulted in a structurally and optoelectronically tunable “dumbbell” structural unit in solution. Single crystals with diverse packing geometries and symmetries will form as the solid assembly of this new supramolecular building block. This supramolecular assembly route introduces a new general strategy for designing halide perovskite structures with potentially new optoelectronic properties.



## INTRODUCTION

The halide perovskite has been the spotlight of semiconductor research in the past decade owing to its superior optoelectronic properties: a high optical absorption coefficient, tunable band gap, long free carrier diffusion length, high defect tolerance, and efficient photo-/electro-luminescence.<sup>1,2</sup> There are increasing studies revealing the fact that the  $[MX_6]^{n-}$  ( $M = Pb^{2+}$ ,<sup>3–5</sup>  $Sb^{3+}$ ,<sup>6–8</sup>  $Te^{4+}$ ,<sup>9–11</sup>  $Sn^{4+}$ ,<sup>12,13</sup>  $Pt^{4+}$ ,<sup>14</sup> etc.;  $X = Cl^-$ ,  $Br^-$ ,  $I^-$ ) metal halide ionic octahedral units are the fundamental building blocks and functional units in metal halide perovskites. To this end, metal halide perovskites can be described as the extended assembly of these octahedra balanced by counter cations.<sup>14,15</sup> In this work, we introduce supramolecular cations as the counter cations for constructing the metal halide octahedron assembly. Crown ethers can readily coordinate with alkali metals to form crown ether@alkali metal cations that have been widely used for supramolecular assembly.<sup>16,17</sup> Various assemblies of polyoxometalate clusters<sup>18</sup> and metal halide clusters, such as the five-coordinate  $[SbX_5]^{2-}$  complex<sup>19</sup> or the four-coordinate  $[FeCl_4]^{-20}$  and  $[MnBr_4]^{2-21}$  complexes, can be formed by employing different crown ether@alkali metal complexes. Here, we show that the assembly of the metal halide octahedron results in a family of unique dumbbell-shaped (crown ether@A)<sub>2</sub>M(IV)X<sub>6</sub> [crown ether = 18-Crown-6 (18C6), 21-Crown-7 (21C7); A = Cs<sup>+</sup>, Rb<sup>+</sup>, and K<sup>+</sup>; M = Te<sup>4+</sup>, Sn<sup>4+</sup>, Se<sup>4+</sup>, Ir<sup>4+</sup>, Pt<sup>4+</sup>, Zr<sup>4+</sup>, and Ce<sup>4+</sup>; and X = Cl<sup>-</sup>, Br<sup>-</sup>, and I<sup>-</sup>] structural units in solution, which can be further packed into various three-dimensional crystal structures.

Moreover, the optoelectronic properties of the resultant assembly can be tuned by using different building units, providing an additional knob for the rational design of functional metal halide perovskites.

Previous studies have shown that upon dissolving bulk A<sub>2</sub>M(IV)X<sub>6</sub> vacancy-ordered double perovskites in polar aprotic solvents, the ionic bond between the  $[M(IV)X_6]^{2-}$  and the alkali metal cations (A<sup>+</sup>) dissociates, and the metal halide octahedral units can be stabilized in solution.<sup>22</sup> Additionally, when 18C6 was dissolved in solution, the strong electrostatic interaction between the alkali metal cations A<sup>+</sup> and the oxygen atoms of 18C6 favored (18C6@A)<sup>+</sup> cation formation.<sup>23,24</sup> Furthermore, we discovered that the  $[M(IV)X_6]^{2-}$  octahedra and the (18C6@A)<sup>+</sup> cations in solution self-assemble into an (18C6@A)<sub>2</sub>M(IV)X<sub>6</sub> dumbbell structural unit, where each octahedron is sandwiched by two (18C6@A)<sup>+</sup> cations (Figure 1). This configuration lays the foundation for solid-state supramolecular assembly. Using the anti-solvent vapor-assisted crystallization method (Figure S1), the dumbbell building blocks packed into a unique rhombohedral lattice (Figure 1), which is different from the face-centered cubic

Received: April 23, 2022

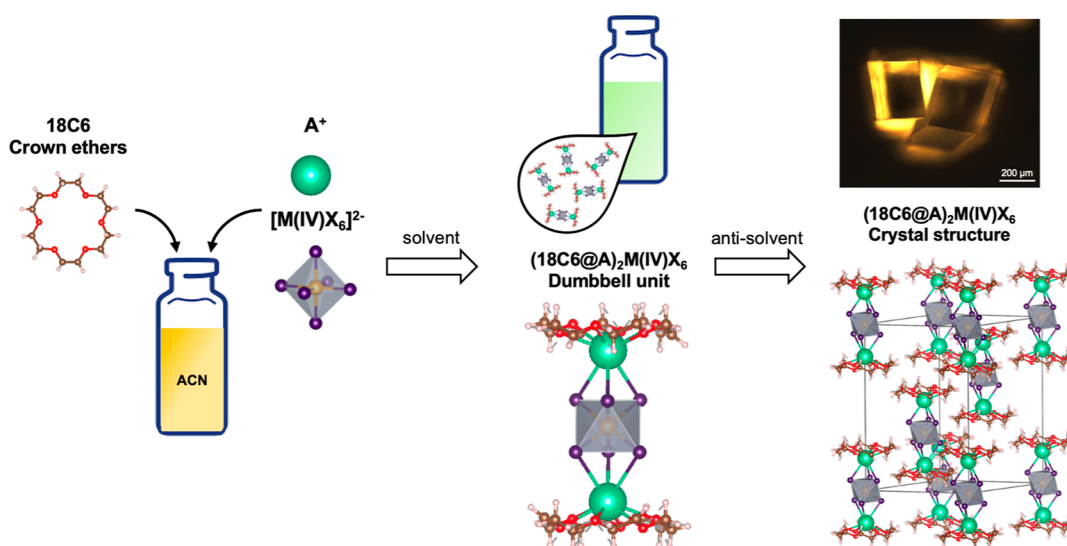


**Figure 1.** Supramolecular assembly strategy from the  $[M(IV)X_6]^{2-}$  octahedron to  $(18C6@A)_2M(IV)X_6$ . The dissolved alkali metal cation ( $A^+$ ) and  $[M(IV)X_6]^{2-}$  octahedron self-assemble into a dumbbell-shaped structural unit with crown ethers like 18-Crown-6 (18C6). The solution-dispersed  $(18C6@A)_2M(IV)X_6$  dumbbell structural units can further assemble into a rhombohedral-packing single crystal. The dark-field optical microscopy image shows single crystals of  $(18C6@Cs)_2Te(IV)Cl_6$ .

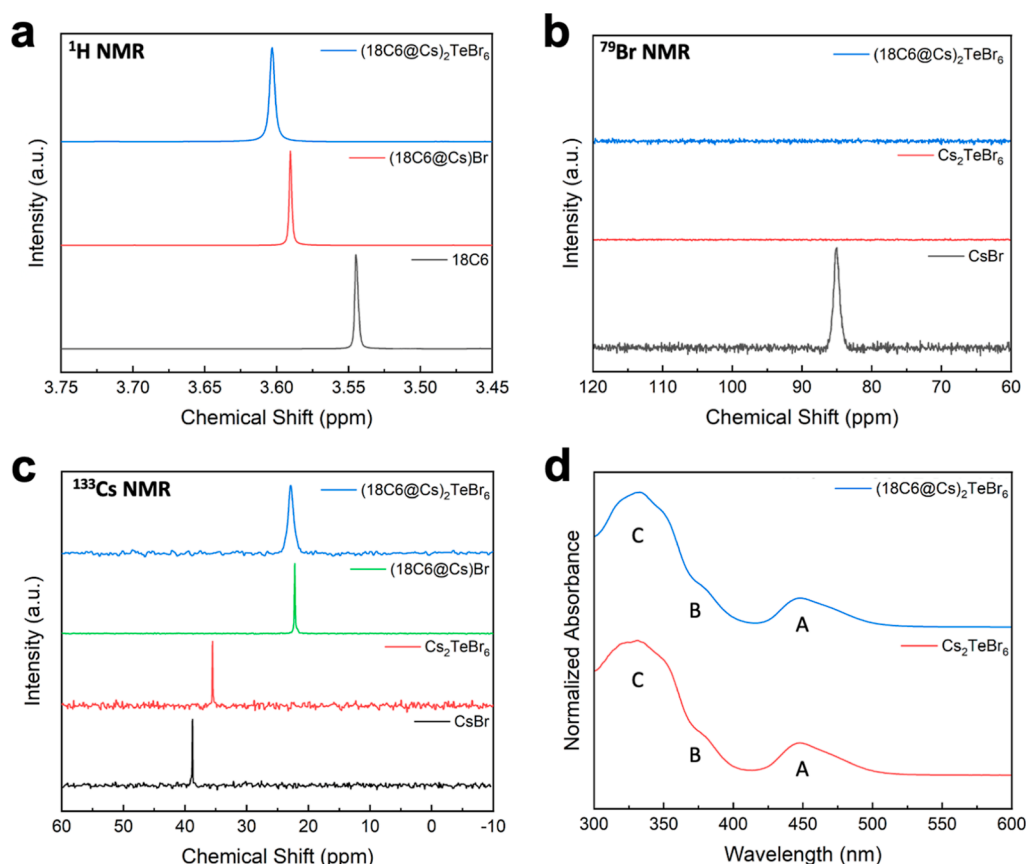


**Figure 2.** Evidence of the formation of the  $(18C6@A)_2M(IV)X_6$  dumbbell structural unit in solution. The composition of  $(18C6@Cs)_2TeBr_6$  is applied as an illustrating example for the dumbbell structural unit, and ACN ( $ACN-d_3$  for NMR) is used as the solvent. (a)  $^1H$  NMR spectra for  $(18C6@Cs)_2TeBr_6$  solution and the control groups are  $(18C6@Cs)Br$  and 18C6 dissolved in solution. (b)  $^{79}Br$  NMR spectra for  $(18C6@Cs)_2TeBr_6$  solution and the control groups are  $Cs_2TeBr_6$  and  $CsBr$  dissolved in solution. (c)  $^{133}Cs$  NMR spectra for  $(18C6@Cs)_2TeBr_6$  solution and the control groups are  $(18C6@Cs)Br$ ,  $Cs_2TeBr_6$ , and  $CsBr$  dissolved in solution. (d) UV-vis spectral comparison of  $(18C6@Cs)_2TeBr_6$  solution and  $Cs_2TeBr_6$  dissolved in ACN solution.

(fcc)-type lattice formed by  $[M(IV)X_6]^{2-}$  and  $A^+$  alone. This new, general synthetic strategy allows us to build up a family of

new supramolecular structures based upon these metal halide octahedral building blocks.

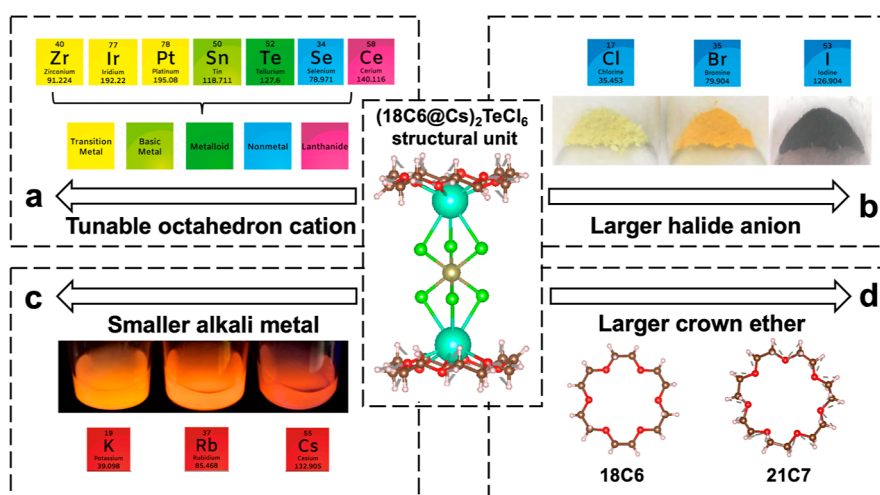


**Figure 3.** Synthetic tunability of the crown ether supramolecular approach. The four arrows represent the four dimensionalities in tuning the dumbbell structural unit from the initial  $(18C6@Cs)_2TeCl_6$  structural unit: (a) seven tetravalent octahedral cations can be applied, including transition metal cations such as  $Zr^{4+}$ ,  $Ir^{4+}$ , and  $Pt^{4+}$ , basic metal cations such as  $Sn^{4+}$ , metalloid cations such as  $Te^{4+}$ , nonmetal cations such as  $Se^{4+}$ , and lanthanide cations such as  $Ce^{4+}$ ; (b) tuning the halide anion from  $Cl^-$  to  $Br^-$  to  $I^-$  and the optical images are the powders of  $(18C6@Cs)_2TeX_6$  ( $X = Cl^-, Br^-, I^-$ ) under ambient light; (c) modifying the alkali metal cation coupled with 18C6 from  $Cs^+$  to  $Rb^+$  to  $K^+$  and the optical images are the powders of  $(18C6@A)_2TeCl_6$  dispersed in an anti-solvent under 365 nm UV lamp excitation; and (d) varying the size of the crown ether from 18C6 to 21C7.

## RESULTS AND DISCUSSION

**Structural Unit Formation in Solution.** The charge-neutral  $(18C6@A)_2M(IV)X_6$  dumbbell structural units are formed by dissolving 18C6 and  $A_2M(IV)X_6$  in acetonitrile (ACN). This was verified using multiple solution-state characterization techniques, using  $(18C6@Cs)_2TeBr_6$  as an illustrating example. The NMR-active  $^1H$ ,  $^{79}Br$ , and  $^{133}Cs$  nuclei in the dumbbell structural unit experience different magnetic fields compared to the isolated nuclei (Figure 2a–c). The 24 homotopic protons on the 18C6 ring have identical NMR absorptions, at around 3.54 ppm in terms of a chemical shift. Once  $Cs^+$  is crowned, due to the partial removal of proton–electron density by the cation, the protons will be deshielded, and the chemical shift will increase to 3.59 ppm (Figure 2a), consistent with reports that  $(18C6@Cs)^+$  exists in ACN.<sup>23</sup> However, with the addition of  $[TeBr_6]^{2-}$  ionic octahedra, the chemical shift is further increased to 3.61 ppm. This increase indicated further withdrawal of electron density from the protons in the presence of  $[TeBr_6]^{2-}$ , which implied attachment to the  $(18C6@Cs)^+$  cations.  $^{79}Br$  NMR revealed strong signals of free  $Br^-$  ions of  $CsBr$  in ACN, while the spin relaxation of  $^{79}Br$  was quenched completely by  $Te^{4+}$  in  $Cs_2TeBr_6$  (Figure 2b) under the same measurement conditions most likely due to quadrupolar interaction.<sup>25</sup>  $(18C6@Cs)_2TeBr_6$  in ACN showed the same quenching behavior as the  $Cs_2TeBr_6$ ; the absence of  $^{79}Br$  NMR signals confirmed that Br was coordinated to  $Te^{4+}$ .

To provide evidence that the dumbbell structural unit exists in ACN,  $^{133}Cs$  NMR (Figure 2c) was also conducted since Cs is the bridging atom that directly coordinates with both, Br of  $[TeBr_6]^{2-}$  and O of 18C6. The free Cs chemical shift of  $CsBr$  was located at 38.81 ppm, while it was located at 35.56 ppm for  $Cs_2TeBr_6$  in ACN. The 3.25 ppm difference in these controls indicated that the presence of  $Te^{4+}$  in the solution caused the peak to shift to lower ppm values. In contrast, a pronounced shielding effect was observed when  $Cs^+$  was crowned into  $(18C6@Cs)^+$  in ACN, which suggested a withdrawal of electron density from the crown ether to  $Cs^+$ , consistent with

the  $^1H$  NMR results. Adding  $[TeBr_6]^{2-}$  into  $(18C6@Cs)^+$  in ACN changed the Cs chemical shift from 22.22 to 22.97 ppm, which supported the formation of a new species, the dumbbell structural unit, distinct from its individual components. The dramatically broadened signal also supported the formation of a dumbbell as dipole–dipole interactions are introduced in slowly tumbling large-molecular weight species. The UV–vis spectrum of  $(18C6@Cs)_2TeBr_6$  precursors in ACN clearly shows the A, B, and C characteristic absorption bands of  $[TeBr_6]^{2-}$  (Figure 2d),<sup>22</sup> indicating the presence of  $[TeBr_6]^{2-}$  in solution. With the comprehensive measurements in  $^1H$ ,  $^{79}Br$ , and  $^{133}Cs$  NMR and UV–vis spectroscopy, we characterized the species in the solution phase, confirming the integrity of the dumbbell structural unit in solution (Figure 1).

**Single-Crystal Characterization.** With the suspension of  $(18C6@A)_2M(IV)X_6$  units in ACN solution, we successfully achieved the solid-state assembly, in the form of single crystals, with the introduction of antisolvents like diethyl ether. For example, the  $(18C6@Cs)_2TeCl_6$  single crystals have a parallelepiped shape, consistent with crystallographic symmetry, with a lateral dimension of approximately 300  $\mu m$  (Figure S2). The structural details of the crystals were determined from single-crystal X-ray diffraction (SCXRD).  $(18C6@Cs)_2TeCl_6$  crystallized in the  $R\bar{3}$  space group with lattice parameters of  $a = 13.9378$  Å and  $c = 22.0396$  Å (Table S1). The  $(18C6@Cs)_2TeCl_6$  dumbbell structural unit belonged to the  $S_6$  point group, where two  $Cs^+$  cations and the  $Te^{4+}$  cation sit on the  $S_6$  axis, and the six-fold symmetry of the 18C6 and the  $S_6$  axis of the  $O_h$ -symmetric  $[TeCl_6]^{2-}$  octahedron were perfectly aligned. In the  $(18C6@Cs)_2TeCl_6$  dumbbell unit, the Te–Cl bond length was determined as 2.546 Å, which was comparable to that in the  $Cs_2TeCl_6$  vacancy-ordered double perovskite (2.570 Å).<sup>9</sup> The high symmetry of this dumbbell building block offered a unique rhombohedral packing of the octahedra at the macroscopic level. Each  $[TeCl_6]^{2-}$  octahedron occupied the b Wyckoff position of space group  $R\bar{3}$  and was surrounded by six nearest octahedra at a Te–Te distance of 10.9 Å, which

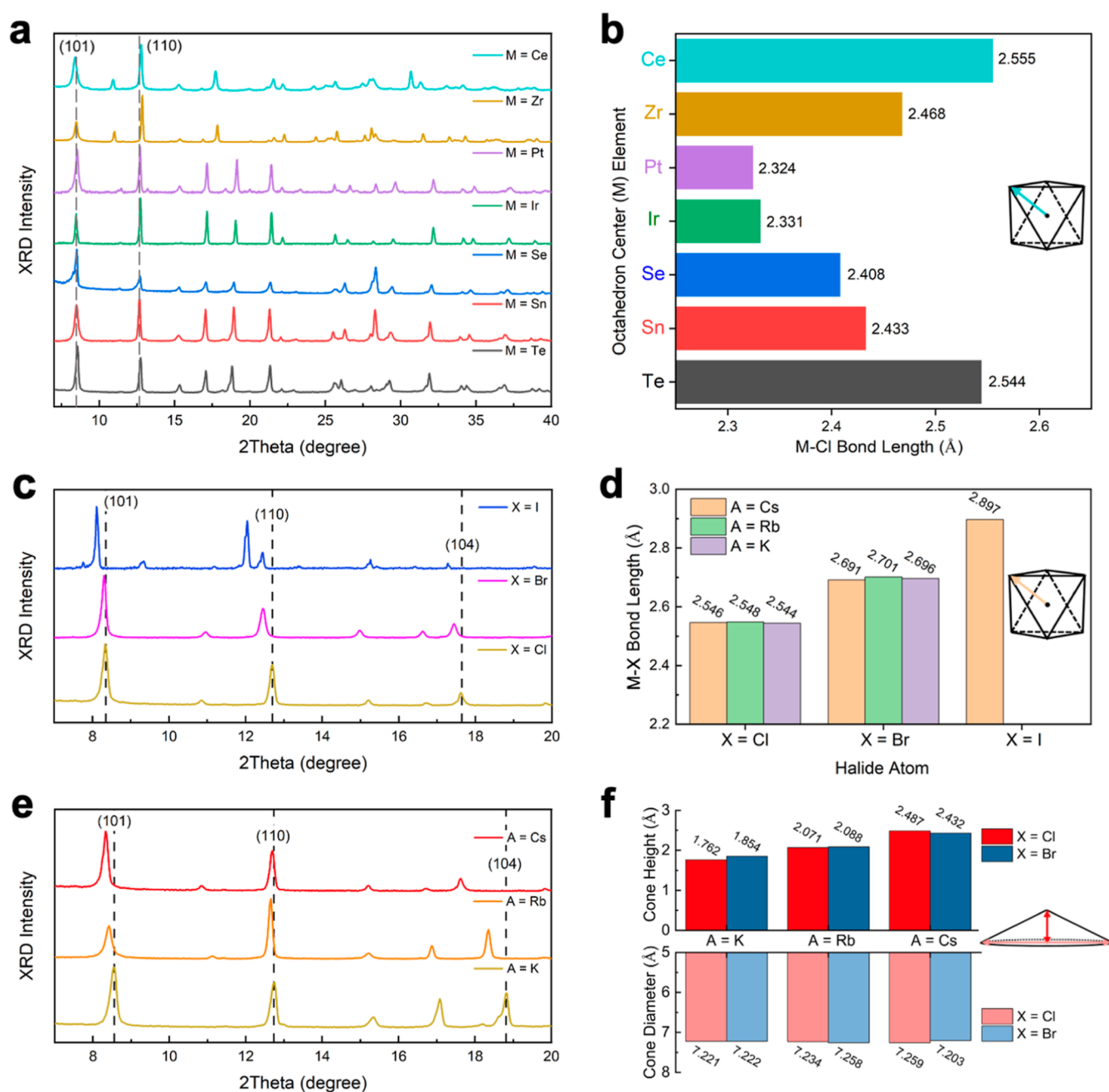


**Figure 4.** Systematic structural analysis of the family of  $(18C6@A)_2M(IV)X_6$  crystals. Comparison of PXRD patterns by (a) tuning the octahedron center element (M) in  $(18C6@A)_2M(IV)Cl_6$  (for M = Ce and Zr and A = Cs; for M = Pt, Ir, Se, Sn, and Te and A = K); (c) changing the halide atom (X) in  $(18C6@Cs)_2TeX_6$ ; and (e) varying the alkali metal atom (A) in  $(18C6@A)_2TeCl_6$ . Analysis of the geometric parameters of the dumbbell structural units: (b) M–Cl bond length comparison of the structures with different octahedron center elements; (d) the M–X bond length increases with larger X; and (f) the height of the cone increases with larger A, while the diameter of the cone is insensitive to the change of A.

was different from the fcc packing in  $Cs_2TeCl_6$  with a Te–Te distance of 7.7 Å.<sup>9</sup> The voids within the lattice are occupied by disordered solvent molecules. These tunable differences in the metal halide octahedron packing geometry may lead to differences in the overlap of molecular orbital wavefunctions, yielding unique electronic structures and optoelectronic properties that will be discussed later.

**Tunability of the Supramolecular Approach.** To demonstrate the general applicability of our approach, we produced various crystals through this supramolecular assembly strategy. In fact, the composition tunability of this

new  $(18C6@A)_2M(IV)X_6$  structure is as rich as the tunabilities on A, M, and X sites in  $A_2M(IV)X_6$  double perovskites.<sup>26</sup> There are four compositional components in the  $(18C6@Cs)_2TeCl_6$  dumbbell structural unit which can be tuned by virtue of the precursors: (a) octahedron cations (M), (b) halide anions (X), (c) alkali metal cations (A), and (d) crown ethers (Figure 3). Apart from  $[TeX_6]^{2-}$ , various tetravalent center cation octahedra, such as  $[SnX_6]^{2-}$ ,  $[SeX_6]^{2-}$ ,  $[PtX_6]^{2-}$ ,  $[ZrX_6]^{2-}$ , and  $[CeX_6]^{2-}$ ,<sup>12,13,27–35</sup> can also be assembled into similar dumbbell structural units with  $S_6$  symmetry. For typical 3D connected halide perovskites, such



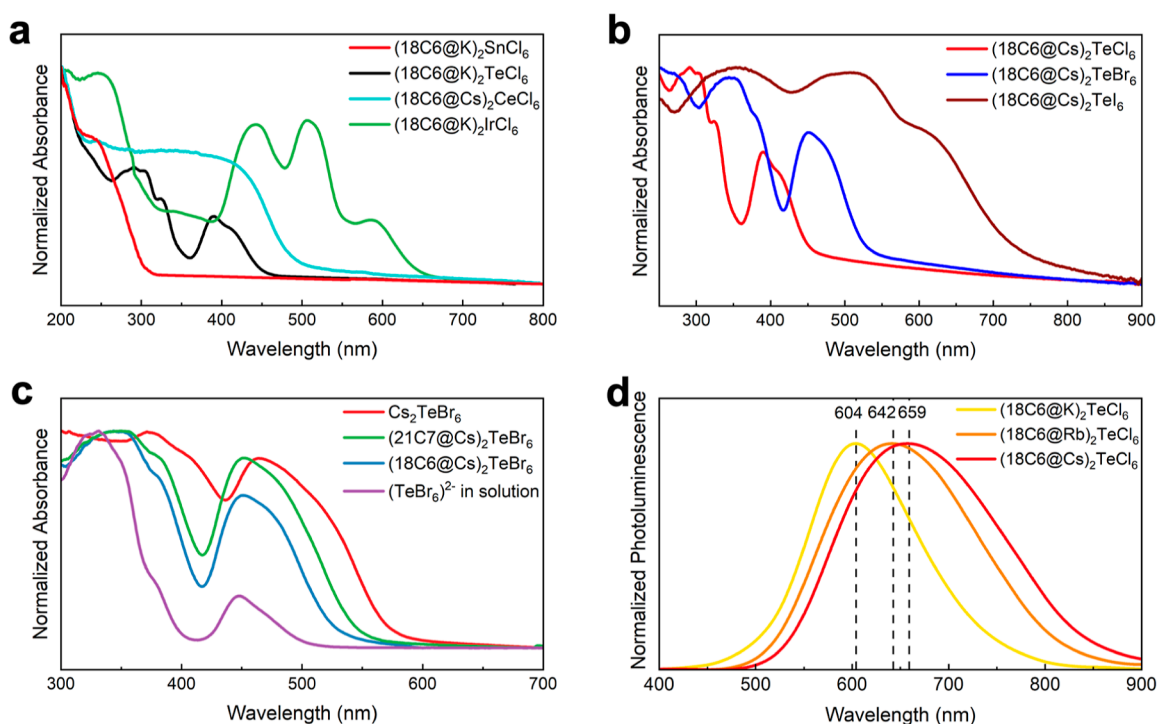


**Figure 5.** Optoelectronic tunability of the crown ether supramolecular approach. (a) Normalized UV-vis absorption spectra of (18C6@A)<sub>2</sub>M(IV)Cl<sub>6</sub> (M = Sn<sup>4+</sup>, Te<sup>4+</sup>, Ce<sup>4+</sup>, and Ir<sup>4+</sup>) crystals. (b) Normalized UV-vis absorption spectra of (18C6@Cs)<sub>2</sub>TeX<sub>6</sub> (X = Cl<sup>-</sup>, Br<sup>-</sup>, and I<sup>-</sup>) crystals. (c) Normalized UV-vis absorption spectra of [TeBr<sub>6</sub>]<sup>2-</sup> octahedra under four different packing geometries. (d) Normalized PL spectra of (18C6@A)<sub>2</sub>TeCl<sub>6</sub> (A = Cs<sup>+</sup>, Rb<sup>+</sup>, and K<sup>+</sup>) crystals.

as low-*T* phase CsPbI<sub>3</sub>,<sup>36</sup> due to the geometrical constraint imposed by the ionic framework sizes, such as the tolerance factor and proper bonding directions, a mismatched ionic size will lead to the breakdown or instability of the perovskite structure.<sup>37</sup> In contrast, the isolated nature of the dumbbell structural units enables a more flexible control over the structure diversity without losing the prototypical crystal structure. Herein, we achieve a variety of unique dumbbell structures with our unique synthetic approach by simply changing the precursors. All structural details of the highly tunable (18C6@A)<sub>2</sub>M(IV)X<sub>6</sub> dumbbell structural units were obtained by powder XRD (PXRD) and SCXRD (Tables S1–S7).

The comparison of PXRD patterns for the seven different octahedron center cations (Te<sup>4+</sup>, Sn<sup>4+</sup>, Se<sup>4+</sup>, Ir<sup>4+</sup>, Pt<sup>4+</sup>, Zr<sup>4+</sup>, and Ce<sup>4+</sup>) is shown in Figure 4a. Despite size differences between the different metal halide octahedral units, represented by the M–Cl bond length (from 2.324 to 2.555 Å) summarized in Figure 4b, they all had similar hexagonal PXRD patterns, with strong and distinct (101) and (110) diffraction peaks. In order to better evaluate the geometry of the dumbbell structural unit with various compositions, we used a simplified model made up of two cones and one octahedron (Figure S3). A larger halide anion (from Cl<sup>-</sup> to Br<sup>-</sup> to I<sup>-</sup>) leads to a larger octahedron size (Figure 4d), and the length of the dumbbell structural unit increases in all three dimensions, reflected by the shifting of all diffraction peaks to lower 2θ values (Figure 4c). Although the bromide version remained in the *R*3̄ space group (Table S2), the iodide version deviated from the hexagonal symmetry and crystallized in the monoclinic crystal system with the space group of *P*2<sub>1</sub>/*m* (Table S7 and Figure S4) due to the larger size of the iodide anion. On the contrary, we found that the MX<sub>6</sub> bonds were not influenced by the alkali

metal cations, and the *R*3̄ space group can be preserved. Figure 4f shows that the Te–Cl bond lengths were 2.546 Å, 2.548 Å, and 2.544 Å for the Cs-, Rb-, and K-based assemblies, respectively. However, when using a smaller alkali cation, the height of the cone decreased (from ~2.4 Å to ~1.8 Å when changing from Cs<sup>+</sup> to K<sup>+</sup>), while the diameter of the cone remained nearly unchanged. This height decrease was consistent with a shift in the diffraction peaks related to the *c* lattice parameter [such as (101) and (104) planes] to larger 2θ values. In contrast, the diffraction of facets parallel to the *c* axis, such as the (110) plane, has almost no shift (Figures 4e and S5 and S6). We also compared the single crystals of (18C6@K)<sub>2</sub>TeBr<sub>6</sub> synthesized from ACN and DMF (Table S8); both crystals are in the *R*3̄ space group and only show slight differences in lattice parameters, which are attributed to the occupation of disordered larger DMF molecules compared to ACN molecules in the voids within the lattice. Thermogravimetric analysis on (18C6@Cs)<sub>2</sub>TeCl<sub>6</sub> shows that the total relative mass changes from 98.5% [*M*<sub>w</sub> = 1248.95 g/mol for (18C6@Cs)<sub>2</sub>TeCl<sub>6</sub>·2DMF] to 88.6% [*M*<sub>w</sub> = 1134.76 g/mol for (18C6@Cs)<sub>2</sub>TeCl<sub>6</sub>] from 80 to 120 °C and further reduced to 48.9% (*M*<sub>w</sub> = 606.13 g/mol for Cs<sub>2</sub>TeCl<sub>6</sub>) from 160 to 220 °C (Figure S7). The same decomposition process is also verified for (18C6@Cs)<sub>2</sub>SnCl<sub>6</sub> and (18C6@Cs)<sub>2</sub>TeBr<sub>6</sub>. Thermal analysis studies reveal the fact that for this family of new materials, the solvent molecules (such as DMF) occupying the lattice voids are evaporated from 80 to 120 °C, and 18C6 starts to detach at roughly 160 °C and completely decomposes into the corresponding all-inorganic Cs<sub>2</sub>MX<sub>6</sub> powders after 220 °C. It also proves the existence of solvent molecules in the lattice voids as we expected from the single-crystal structure studies.

To further confirm the intact  $O_h$  symmetry of the metal halide octahedral building blocks, we used Raman spectroscopy to study the vibrational modes of the dumbbell structural unit. Previous Raman studies of the  $Cs_2TeCl_6$  crystal system determined that the vibrational units in the single crystals were the isolated  $[TeCl_6]^{2-}$  octahedra with  $O_h$  point group symmetry (Figure S8).<sup>9</sup> All three characteristic Raman peaks were still observed in the  $(18C6@A)_2TeCl_6$  single crystals (Figure S9), confirming the  $O_h$  symmetry of the  $[TeCl_6]^{2-}$  unit in the dumbbell building block. Similar  $O_h$ -symmetry Raman peaks were also observed in assembled crystals with other octahedra, such as  $[TeBr_6]^{2-}$ ,  $[SnCl_6]^{2-}$ , and  $[SnBr_6]^{2-}$  (Figures S10–S12).

The compatibility between the point groups of 18C6 and the metal halide octahedral units resulted in the rhombohedral  $R\bar{3}$  space group of the assembled single crystals. By breaking the six-fold symmetry of the crown ether, the supramolecular approach can realize more packing geometries for these metal halide octahedral units. For example, the larger 21-Crown-7 (21C7) had to distort itself to coordinate with the center  $Cs^+$  cation (Figure S13a). Such distortion of the dumbbell building block dramatically altered the packing geometry of these building blocks (Figure S13b, c). Single crystals of  $(21C7@Cs)_2TeBr_6$  and  $(21C7@Cs)_2TeI_6$  crystallized in an orthorhombic lattice with space group  $Cmc2_1$  (Table S9). The  $[TeBr_6]^{2-}$  units in the  $(21C7@Cs)_2TeBr_6$  dumbbell unit were still nearly perfect, but this distorted dumbbell structure was found to be horizontally packed into a two-dimensional (2D) array form. In each  $[TeBr_6]^{2-}$  octahedral plane, one octahedron had four nearest neighbors (the Te–Te distance is 9.9 Å), with no solvent molecules or crown ether complexes in between. The interlayer spacing of the 2D octahedral sheets was about 13.7 Å. Consistent with a 2D structure, the (002) diffraction peak was much stronger than the other diffraction peaks (Figure S14). The single crystal had a planar shape with a width of over 400  $\mu m$  and a thickness of only 35  $\mu m$  (Figures S15 and S16). Therefore, the use of 21C7 introduced another new type of metal halide octahedral unit packing in our supramolecular assemblies.

**Optoelectronic Properties of the Supramolecular Assemblies.** The demonstrated synthetic flexibility and systematic control of the crystal structures assembled from the dumbbell structural unit have deep implications for their electronic properties. The electronic structure of the structural unit is primarily determined by the metal halide octahedral units.<sup>14</sup> For instance, by tuning the center metal cation of the  $[M(IV)X_6]^{2-}$  ( $M = Sn^{4+}$ ,  $Te^{4+}$ ,  $Ce^{4+}$ , and  $Ir^{4+}$ ) ionic octahedron, the optical absorption onset of the supramolecular-assembled crystals varied from 660 nm for  $[IrCl_6]^{2-}$  to 500 nm for  $[CeCl_6]^{2-}$ , to 460 nm for  $[TeCl_6]^{2-}$ , and to 310 nm for  $[SnCl_6]^{2-}$  (Figure 5a). The differences in absorption features for these four ionic octahedra are due to their different electronic configurations.  $Te^{4+}$  is a cation with  $ns^2$  electronic configuration; the absorbance of  $[TeCl_6]^{2-}$  octahedra was dominated by the molecular  $S_s$  to  $S_sSp$  transitions, represented as the A, B, and C bands.<sup>38</sup> Recent studies suggested that a sharp absorption band in the UV range for  $[SnCl_6]^{2-}$  can be assigned to a ligand-to-metal charge transfer (LMCT) transition.<sup>28,29</sup> The absorption band was also assigned to the LMCT transition for  $[CeCl_6]^{2-}$ .<sup>39</sup> For Ir, the subshells of the 5d orbitals of  $Ir^{4+}$  in  $[IrCl_6]^{2-}$  contributed to the weak optical transition bands, and intense bands were due to metal–ligand interactions.<sup>40</sup> Changing the halide anions

also contributed to different optical absorptions.  $(18C6@Cs)_2TeX_6$  ( $X = Cl^-$ ,  $Br^-$ ,  $I^-$ ) structural units have vastly different optical absorption features due to the shift of the atomic orbital energy levels of halide anions (Figure 5b).

The optoelectronic tunability of the dumbbell unit can be achieved not only by incorporating various  $[M(IV)X_6]^{2-}$  ionic octahedra but also by changing the octahedral packing geometries and the surrounding coordination environment of the same metal halide octahedra. The electronic interaction of these octahedral units has deep implications for the electronic structure of the crystal. According to the tight-binding model, the superposition of wavefunctions for isolated atoms will be greater when atoms are brought closer together in a solid, so the electronic bands will be more dispersive, and the band gap will decrease.<sup>41</sup> In the current materials system, the individual octahedron can be viewed as a super ion/atom with specific molecular orbital levels. When the octahedra of these dumbbell units are closer to each other, their orbital wavefunctions will overlap to a greater extent. This was confirmed by our experimental observation. The UV–vis absorption spectra of four different packing geometries of the  $[TeBr_6]^{2-}$  octahedra are shown in Figure 5c. As the  $[TeBr_6]^{2-}$  octahedra were packed closer in a crystal by using different crown ether complexes, the A-band absorption onset red-shifted from 500 to 590 nm, causing the crystal to change color from orange  $[(18C6@Cs)_2TeBr_6]$  and  $(21C7@Cs)_2TeBr_6$  to red  $[Cs_2TeBr_6]$  (Figure S17).

The supramolecular-assembled crystals have not only tunable optical absorption but also strong photoluminescence (PL) with a highly tunable emission color. For instance, under 250 nm excitation,  $(18C6@Cs)_2ZrCl_6$  displays an intense blue emission at 459 nm, with a full width at half-maximum (fwhm) of 0.90 eV. The PL quantum yield of  $(18C6@Cs)_2ZrCl_6$  is 12.57%, which is calculated from integrating sphere measurements. Apart from high emission intensities, the supramolecular approach can also enable the fine-tuning of the emission color. The strong coupling of the exciton with lattice vibrations will greatly lower the energy level of the exciton, forcing it into transient self-trapped exciton (STE) states with a range of self-trapped energy levels.<sup>11,30,31,42,43</sup> The  $[TeCl_6]^{2-}$  octahedron was selected to study the STE emission of the dumbbell structural units. The PL spectra (Figures 5d and S18) of the  $(18C6@A)_2TeCl_6$  ( $A = K^+$ ,  $Rb^+$ , and  $Cs^+$ ) crystals had emission peak wavelengths at 604, 642, and 659 nm, respectively. They all featured a large Stokes shift of 1.13, 1.26, and 1.31 eV, respectively, and a very large broadband emission. The PL fwhm was 0.44, 0.54, and 0.55 eV, respectively. The Stokes shift was larger than that of the  $Cs_2TeCl_6$  crystal, with a value of 1.04 eV,<sup>9</sup> which indicated a greater exciton–phonon coupling effect.<sup>42,43</sup> Furthermore, the Stokes shift increased with increasing alkali metal cation size. This phenomenon was likely due to the difference in the alkali metal halide bond strength. A weaker or softer alkali metal halide bond will force the excitonic state into deeper self-trapped levels. The PL studies demonstrate that the supramolecular assembly approach can be used to design emissive and tunable emitters.

## CONCLUSIONS

In conclusion, we demonstrated a general synthetic strategy for a library of new supramolecular building blocks (crown-ether@ $A$ ) $_2M(IV)X_6$ , constructed from ionic halide perovskite octahedral units and crown ethers. The great tunability of (crown-ether@ $A$ ) $_2M(IV)X_6$  can be explored along (1)

changing the octahedron cation, (2) tuning the halide anion, (3) modifying the alkali metal cation coupled with the crown ether, and (4) varying the size of the crown ether. In the future, based on the structural diversity of the supramolecular assembly approach, we expect to extend to one-dimensional and 2D electronic dimensionality solid assembly with connected  $[MX_6]^{n-}$  octahedra. Also, with all these synthetic possibilities, a more in-depth study of the optoelectronic properties of the ionic octahedral building blocks can be conducted. We expect that this new assembly strategy of the supramolecular building blocks could bring a new general method for halide perovskite material discovery.

## ■ ASSOCIATED CONTENT

### SI Supporting Information

The Supporting Information is available free of charge at <https://pubs.acs.org/doi/10.1021/jacs.2c04357>.

Description of experimental details and additional characterization data, single-crystal XRD crystallographic results, schematics, optical images, SEM images, single-crystal XRD, and PXRD characterizations, Raman spectra, UV-vis spectra, and PL spectra (PDF)

The crystallographic information file (CIF) has also been deposited in the Inorganic Crystal Structure Database under reference numbers CSD 2122190-2122206 and 2145197-2145199. These data can be obtained free of charge via <https://www.ccdc.cam.ac.uk/structures/> or by emailing [data\\_request@ccdc.cam.ac.uk](mailto:data_request@ccdc.cam.ac.uk).

### Accession Codes

CCDC 2122190–2122206 and 2145197–2145199 contain the supplementary crystallographic data for this paper. These data can be obtained free of charge via [www.ccdc.cam.ac.uk/data\\_request/cif](http://www.ccdc.cam.ac.uk/data_request/cif), or by emailing [data\\_request@ccdc.cam.ac.uk](mailto:data_request@ccdc.cam.ac.uk), or by contacting The Cambridge Crystallographic Data Centre, 12 Union Road, Cambridge CB2 1EZ, UK; fax: +44 1223 336033.

## ■ AUTHOR INFORMATION

### Corresponding Author

**Peidong Yang** – Department of Materials Science and Engineering and Department of Chemistry, University of California, Berkeley, California 94720, United States; Materials Sciences Division, Lawrence Berkeley National Laboratory, Berkeley, California 94720, United States; Kavli Energy NanoScience Institute, Berkeley, California 94720, United States; [orcid.org/0000-0003-4799-1684](https://orcid.org/0000-0003-4799-1684); Email: [p\\_yang@berkeley.edu](mailto:p_yang@berkeley.edu)

### Authors

**Cheng Zhu** – Department of Materials Science and Engineering, University of California, Berkeley, California 94720, United States; Materials Sciences Division, Lawrence Berkeley National Laboratory, Berkeley, California 94720, United States; [orcid.org/0000-0001-6649-7812](https://orcid.org/0000-0001-6649-7812)

**Jianbo Jin** – Department of Chemistry, University of California, Berkeley, California 94720, United States; [orcid.org/0000-0002-9054-7960](https://orcid.org/0000-0002-9054-7960)

**Mengyu Gao** – Department of Materials Science and Engineering, University of California, Berkeley, California 94720, United States; Materials Sciences Division, Lawrence

Berkeley National Laboratory, Berkeley, California 94720, United States; [orcid.org/0000-0003-1385-7364](https://orcid.org/0000-0003-1385-7364)

**Alexander M. Oddo** – Department of Chemistry, University of California, Berkeley, California 94720, United States; Materials Sciences Division, Lawrence Berkeley National Laboratory, Berkeley, California 94720, United States

**Maria C. Folgueras** – Department of Materials Science and Engineering, University of California, Berkeley, California 94720, United States; Materials Sciences Division, Lawrence Berkeley National Laboratory, Berkeley, California 94720, United States; [orcid.org/0000-0001-6502-7616](https://orcid.org/0000-0001-6502-7616)

**Ye Zhang** – Department of Chemistry, University of California, Berkeley, California 94720, United States; [orcid.org/0000-0001-5953-2173](https://orcid.org/0000-0001-5953-2173)

**Chung-Kuan Lin** – Department of Chemistry, University of California, Berkeley, California 94720, United States; Materials Sciences Division, Lawrence Berkeley National Laboratory, Berkeley, California 94720, United States; [orcid.org/0000-0001-9193-2345](https://orcid.org/0000-0001-9193-2345)

Complete contact information is available at: <https://pubs.acs.org/10.1021/jacs.2c04357>

### Author Contributions

\*C.Z., J.J., and M.G. made equal contribution to this study.

### Notes

The authors declare no competing financial interest.

## ■ ACKNOWLEDGMENTS

The authors thank Dr. Hao Lyu, Dr. Xiaokun Pei, Dr. Chang Yan, Dr. Sheena Louisia, and Zichao Rong for helpful discussions. This work was supported by the U.S. Department of Energy, Office of Science, Office of Basic Energy Sciences, Materials Sciences and Engineering Division, under contract no. DE-AC02-05-CH11231 within the Physical Chemistry of Inorganic Nanostructures program (KC3103). Single-crystal X-ray Diffraction studies were performed at the UC Berkeley College of Chemistry X-ray Crystallography (CheXray). We thank Dr. Nick Settineri at UC Berkeley for his help in SCXRD collection. Ultra-low-frequency Raman spectroscopy was performed at the Stanford Nano Shared Facilities (SNSF), supported by the National Science Foundation (ECCS-2026822). We thank Drs. Hasan Celik, Alicia Lund, and UC Berkeley's NMR facility in the College of Chemistry (CoC-NMR) for spectroscopic assistance. Instruments in CoC-NMR are supported in part by NIH S10OD024998. J.J. and Y.Z. acknowledge the fellowship support from the Suzhou Industrial Park. C.-K.L. acknowledges the MOE Technologies Incubation Scholarship from Taiwan.

## ■ REFERENCES

- (1) Protesescu, L.; Yakunin, S.; Bodnarchuk, M. I.; Krieg, F.; Caputo, R.; Hendon, C. H.; Yang, R. X.; Walsh, A.; Kovalenko, M. V. Nanocrystals of Cesium Lead Halide Perovskites ( $\text{CsPbX}_3$ , X = Cl, Br, and I): Novel Optoelectronic Materials Showing Bright Emission with Wide Color Gamut. *Nano Lett.* **2015**, *15*, 3692–3696.
- (2) Kang, J.; Wang, L.-W. High Defect Tolerance in Lead Halide Perovskite  $\text{CsPbBr}_3$ . *J. Phys. Chem. Lett.* **2017**, *8*, 489–493.
- (3) Kovalenko, M. V.; Protesescu, L.; Bodnarchuk, M. I. Properties and Potential Optoelectronic Applications of Lead Halide Perovskite Nanocrystals. *Science* **2017**, *358*, 745–750.
- (4) Zhang, Y.; Saidaminov, M. I.; Dursun, I.; Yang, H.; Murali, B.; Alarousu, E.; Yengel, E.; Alshankiti, B. A.; Bakr, O. M.; Mohammed,



- O. F. Zero-Dimensional  $\text{Cs}_4\text{PbBr}_6$  Perovskite Nanocrystals. *J. Phys. Chem. Lett.* **2017**, *8*, 961–965.
- (5) Noel, N. K.; Abate, A.; Stranks, S. D.; Parrott, E. S.; Burlakov, V. M.; Goriely, A.; Snaith, H. J. Enhanced Photoluminescence and Solar Cell Performance via Lewis Base Passivation of Organic Inorganic Lead Halide Perovskites. *ACS Nano* **2014**, *8*, 9815–9821.
- (6) Morad, V.; Yakunin, S.; Benin, B. M.; Shynkarenko, Y.; Grotevent, M. J.; Shorubalko, I.; Boehme, S. C.; Kovalenko, M. V. Hybrid 0D Antimony Halides as Air-Stable Luminophores for High Spatial-Resolution Remote Thermography. *Adv. Mater.* **2021**, *33*, 2007355.
- (7) Boopathi, K. M.; Karuppuswamy, P.; Singh, A.; Hanmandlu, C.; Lin, L.; Abbas, S. A.; Chang, C. C.; Wang, P. C.; Li, G.; Chu, C. W. Solution-Processable Antimony-Based Light-Absorbing Materials Beyond Lead Halide Perovskites. *J. Mater. Chem. A* **2017**, *5*, 20843–20850.
- (8) Sedakova, T. V.; Mirochnik, A. G.; Karasev, V. E. Structure and Luminescence Properties of Antimony (III) Complex Compounds. *Opt. Spectrosc.* **2008**, *105*, 517–523.
- (9) Folgueras, M. C.; Jin, J.; Gao, M.; Quan, L. N.; Steele, J. A.; Srivastava, S.; Ross, M. B.; Zhang, R.; Seeler, F.; Schierle-Arndt, K.; Asta, M.; Yang, P. Lattice Dynamics and Optoelectronic Properties of Vacancy-Ordered Double Perovskite  $\text{Cs}_2\text{TeX}_6$  ( $X = \text{Cl}, \text{Br}, \text{I}$ ) Single Crystals. *J. Phys. Chem. C* **2021**, *125*, 25126–25139.
- (10) Ju, D.; Zheng, X.; Yin, J.; Qiu, Z.; Türedi, B.; Liu, X.; Dang, Y.; Cao, B.; Mohammed, O. F.; Bakr, O. M.; Tao, X. Tellurium-Based Double Perovskites  $\text{A}_2\text{TeX}_6$  with Tunable Band Gap and Long Carrier Diffusion Length for Optoelectronic Applications. *ACS Energy Lett.* **2019**, *4*, 228–234.
- (11) Nicholas, A. D.; Walusiak, B. W.; Garman, L. C.; Huda, M. N.; Cahill, C. L. Impact of Noncovalent Interactions on Structural and Photophysical Properties of Zero-Dimensional Tellurium (IV) Perovskites. *J. Mater. Chem. C* **2021**, *9*, 3271–3286.
- (12) Zhou, J.; Luo, J.; Rong, X.; Wei, P.; Molokeyev, M. S.; Huang, Y.; Zhao, J.; Liu, Q.; Zhang, X.; Tang, J.; Xia, Z. Lead-Free Perovskite Variant  $\text{Cs}_2\text{SnCl}_{6-x}\text{Br}_x$  Single Crystals for Narrowband Photodetectors. *Adv. Opt. Mater.* **2019**, *7*, 1900139.
- (13) Yin, H.; Chen, J.; Guan, P.; Zheng, D.; Kong, Q.; Yang, S.; Zhou, P.; Yang, B.; Pullerits, T.; Han, K. Controlling Photoluminescence and Photocatalysis Activities in Lead-Free  $\text{Cs}_2\text{Pt}_{1-x}\text{Sn}_x\text{Cl}_6$  Perovskites via Ion Substitution. *Angew. Chem.* **2021**, *60*, 22693–22699.
- (14) Jin, J.; Folgueras, M. C.; Gao, M.; Yu, S.; Louisia, S.; Zhang, Y.; Quan, L. N.; Chen, C.; Zhang, R.; Seeler, F.; Schierle-Arndt, K.; Yang, P. A New Perspective and Design Principle for Halide Perovskites: Ionic Octahedron Network (ION). *Nano Lett.* **2021**, *21*, 5415–5421.
- (15) Gao, M.; Zhang, Y.; Lin, Z.; Jin, J.; Folgueras, M. C.; Yang, P. The Making of a Reconfigurable Semiconductor with a Soft Ionic Lattice. *Matter* **2021**, *4*, 3874–3896.
- (16) Cram, D. J. The Design of Molecular Hosts, Guests, and Their Complexes. *Angew. Chem., Int. Ed. Engl.* **1988**, *27*, 1009–1020.
- (17) Pedersen, C. J. The Discovery of Crown Ethers. *Angew. Chem.* **1988**, *100*, 1053–1059.
- (18) Akutagawa, T.; Endo, D.; Noro, S.; Cronin, L.; Nakamura, T. Directing Organic-Inorganic hybrid Molecular-Assemblies of Polyoxometalate Crown-Ether Complexes with Supramolecular Cations. *Coord. Chem. Rev.* **2007**, *251*, 2547–2561.
- (19) Morad, V.; Yakunin, S.; Kovalenko, M. V. Supramolecular Approach for Fine-Tuning of the Bright Luminescence from Zero-Dimensional Antimony (III) Halides. *ACS Mater. Lett.* **2020**, *2*, 845–852.
- (20) Rogers, R. D.; Song, Y. The Crystal Structure of a Heterobimetallic Crown Ether Complex:  $[\text{Na}(\text{dibenzo-18-crown-6})][\text{FeCl}_4]$ . *J. Chem. Crystallogr.* **1995**, *25*, 579–582.
- (21) Hausmann, D.; Kuzmanoski, A.; Feldmann, C.  $\text{MnBr}_2/18$ -Crown-6 Coordination Complexes Showing High Room Temperature Luminescence and Quantum Yield. *Dalton Trans.* **2016**, *45*, 6541–6547.
- (22) Folgueras, M. C.; Louisia, S.; Jin, J.; Gao, M.; Du, A.; Fakra, S. C.; Zhang, R.; Seeler, F.; Schierle-Arndt, K.; Yang, P. Ligand-Free Processable Perovskite Semiconductor Ink. *Nano Lett.* **2021**, *21*, 8856–8862.
- (23) Hopkins, H. P., Jr.; Norman, A. B. Conductance and Infrared Studies on Acetonitrile Solutions Containing Crown Ethers and Alkali Metal Salts. *J. Phys. Chem.* **1980**, *84*, 309–314.
- (24) Shamsipur, M.; Saeidi, M. Conductance Study of Binding of Some  $\text{Rb}^+$  and  $\text{Cs}^+$  Ions by Macrocyclic Polyethers in Acetonitrile Solution. *J. Solut. Chem.* **2000**, *29*, 1187–1198.
- (25) Peng, L.; Clément, R. J.; Lin, M.; Yang, Y. NMR Principles of Paramagnetic Materials. In *NMR and MRI of Electrochemical Energy Storage Materials and Devices*; Royal Society of Chemistry, 2021; CHAPTER 1, pp 1–70.
- (26) Maughan, A. E.; Ganose, A. M.; Scanlon, D. O.; Neilson, J. R. Perspectives and Design Principles of Vacancy-Ordered Double Perovskite Halide Semiconductors. *Chem. Mater.* **2019**, *31*, 1184–1195.
- (27) Faizan, M.; Bhamu, K. C.; Murtaza, G.; He, X.; Kulhari, N.; Al-Anazy, M. M.; Khan, S. H. Electronic and Optical Properties of Vacancy Ordered Double Perovskites  $\text{A}_2\text{BX}_6$  ( $\text{A} = \text{Rb}, \text{Cs}$ ;  $\text{B} = \text{Sn}, \text{Pd}, \text{Pt}$ ; and  $\text{X} = \text{Cl}, \text{Br}, \text{I}$ ): a First Principles Study. *Sci. Rep.* **2021**, *11*, 6965.
- (28) BelhajSalah, S.; Abdelbaky, M. S. M.; García-Granda, S.; Essalah, K.; Ben Nasr, C.; Mrad, M. L. Crystal Structure, Hirshfeld Surfaces Computational Study and Physicochemical Characterization of the Hybrid Material  $(\text{C}_7\text{H}_{10}\text{N})_2[\text{SnCl}_6]\cdot\text{H}_2\text{O}$ . *J. Mol. Struct.* **2018**, *1152*, 276–286.
- (29) Mathlouthi, M.; Valkonen, A.; Rzaigui, M.; Smirani, W. Structural Characterization, Spectroscopic, Thermal, AC Conductivity and Dielectric Properties and Antimicrobial Studies of  $(\text{C}_8\text{H}_{12}\text{N})_2[\text{SnCl}_6]$ . *Phase Transitions* **2017**, *90*, 399–414.
- (30) Tan, Z.; Chu, Y.; Chen, J.; Li, J.; Ji, G.; Niu, G.; Gao, L.; Xiao, Z.; Tang, J. Lead-Free Perovskite Variant Solid Solutions  $\text{Cs}_2\text{Sn}_{1-x}\text{Te}_x\text{Cl}_6$ : Bright Luminescence and High Anti-Water Stability. *Adv. Mater.* **2020**, *32*, 2002443.
- (31) Li, M.; Xia, Z. Recent Progress of Zero-Dimensional Luminescent Metal Halides. *Chem. Soc. Rev.* **2021**, *50*, 2626–2662.
- (32) Hesse, K.; Gliemann, G. Magnetic Field Effect on the Luminescence of Octahedral Hexachloroselenate (IV). Evidence for the Vibronic Nature of the Low-Temperature Emission. *J. Phys. Chem.* **1991**, *95*, 95–98.
- (33) Kaatz, T.; Marcovich, M. The Crystal Structure of the Compound  $\text{Cs}_2\text{CeCl}_6$ . *Acta Crystallogr.* **1966**, *21*, 1011.
- (34) Saeki, K.; Fujimoto, Y.; Koshimizu, M.; Yanagida, T.; Asai, K. Comparative Study of Scintillation Properties of  $\text{Cs}_2\text{HfCl}_6$  and  $\text{Cs}_2\text{ZrCl}_6$ . *Appl. Phys. Express* **2016**, *9*, 042602.
- (35) Khan, N.; Prishchenko, D.; Skourski, Y.; Mazurenko, V. G.; Tsirlin, A. A. Cubic Symmetry and Magnetic Frustration on the FCC Spin Lattice in  $\text{K}_2\text{IrCl}_6$ . *Phys. Rev. B* **2019**, *99*, 144425.
- (36) Lin, Z.; Zhang, Y.; Gao, M.; Steele, J. A.; Louisia, S.; Yu, S.; Quan, L. N.; Lin, C.-K.; Limmer, D. T.; Yang, P. Kinetics of Moisture-Induced Phase Transformation in Inorganic Halide Perovskite. *Matter* **2021**, *4*, 2392–2402.
- (37) Goldschmidt, V. M. Die Gesetze der Krystallochemie. *Naturwissenschaften* **1926**, *14*, 477–485.
- (38) Vogler, A.; Nikol, H. The Structures of  $s^2$  Metal Complexes in the Ground and  $sp$  Excited States. *Comments Inorg. Chem.* **1993**, *14*, 245–261.
- (39) Yin, H.; Jin, Y.; Hertzog, J. E.; Mullane, K. C.; Carroll, P. J.; Manor, B. C.; Anna, J. M.; Schelter, E. J. The Hexachloroacetate (III) Anion: a Potent, Benchtop Stable, and Readily Available Ultraviolet Photosensitizer for Aryl Chlorides. *J. Am. Chem. Soc.* **2016**, *138*, 16266–16273.
- (40) Machmer, P. On the Correlation of  $^{35}\text{Cl}$  Nuclear Quadrupole Coupling Constants with  $\pi \rightarrow \gamma_3$  and  $\pi \rightarrow \gamma_5$  Optical Electron Transfer Bands of Transition Metal Complexes and its Significance in  $\pi$ -bonding. *Z. Naturforsch., B: Anorg. Chem., Org. Chem., Biochem., Biophys., Biol.* **1969**, *24*, 193–199.



- (41) Boyer-Richard, S.; Katan, C.; Traoré, B.; Scholz, R.; Jancu, J.-M.; Even, J. Symmetry-Based Tight Binding Modeling of Halide Perovskite Semiconductors. *J. Phys. Chem. Lett.* **2016**, *7*, 3833–3840.
- (42) Biswas, A.; Bakthavatsalam, R.; Bahadur, V.; Biswas, C.; Mali, B. P.; Raavi, S. S. K.; Gonnade, R. G.; Kundu, J. Lead-Free Zero-Dimensional Tellurium (IV) Chloride-Organic Hybrid with Strong Room Temperature Emission as a Luminescent Material. *J. Mater. Chem. C* **2021**, *9*, 4351–4358.
- (43) Steele, J. A.; Puech, P.; Keshavarz, M.; Yang, R.; Banerjee, S.; Debroye, E.; Kim, C. W.; Yuan, H.; Heo, N. H.; Vanacken, J.; Walsh, A.; Hofkens, J.; Roeffaers, M. B. J. Giant Electron-Phonon Coupling and Deep Conduction Band Resonance in Metal Halide Double Perovskite. *ACS Nano* **2018**, *12*, 8081–8090.